LOFAR early-time search for coherent radio emission from short GRB 181123B

Rowlinson, A.; Starling, R.L.C.; Gourdji, K.; Anderson, G.E.; ter Veen, S.; Mandhai, S.; Wijers, R.A.M.J.; Shimwell, T.W.; van der Horst, A.J.

DOI
10.1093/mnras/stab2060

Publication date
2021

Document Version
Final published version

Published in
Monthly Notices of the Royal Astronomical Society

Monthly Notices of the ROYAL ASTRONOMICAL SOCIETY

MNRAS **506,** 5268–5277 (2021) https://doi.org/10.1093/mnras/stab2060
Advance Access publication 2021 July 21

LOFAR early-time search for coherent radio emission from short GRB 181123B

A. Rowlinson [1,2]★ R. L. C. Starling [3] K. Gourdji [1] G. E. Anderson [4] S. ter Veen,[2] S. Mandhai,[3] R. A. M. J. Wijers [1] T. W. Shimwell[2] and A. J. van der Horst[5,6]

[1]*Anton Pannekoek Institute, University of Amsterdam, Postbus 94249, 1090 GE Amsterdam, the Netherlands*
[2]*ASTRON, the Netherlands Institute for Radio Astronomy, Oude Hoogeveensedijk 4, 7991 PD, Dwingeloo, the Netherlands*
[3]*School of Physics and Astronomy, University of Leicester, University Road, Leicester LE1 7RH, UK*
[4]*International Centre for Radio Astronomy Research, Curtin University, GPO Box U1987, Perth, WA 6845, Australia*
[5]*Department of Physics, The George Washington University, 725 21st Street NW, Washington, DC 20052, USA*
[6]*Astronomy, Physics, and Statistics Institute of Sciences (APSIS), 725 21st Street NW, Washington, DC 20052, USA*

Accepted 2021 July 14. Received 2021 June 22; in original form 2020 August 28

ABSTRACT

The mergers of two neutron stars are typically accompanied by broad-band electromagnetic emission from either a relativistic jet or a kilonova. It has also been long predicted that coherent radio emission will occur during the merger phase or from a newly formed neutron star remnant; however, this emission has not been seen to date. This paper presents the deepest limits for this emission from a neutron star merger, following triggered LOFAR observations of the short gamma-ray burst 181123B, starting 4.4 min after the GRB occurred. During the X-ray plateau phase, a signature of ongoing energy injection, we detect no radio emission to a 3σ limit of 153 mJy at 144 MHz (image integration time of 136 s), which is significantly fainter than the predicted emission from a standard neutron star. At a redshift of 1.8, this corresponds to a luminosity of 2.5×10^{44} erg s^{-1}. Snapshot images were made of the radio observation on a range of time-scales, targeting short-duration radio flashes similar to fast radio bursts. No emission was detected in the snapshot images at the location of GRB 181123B enabling constraints to be placed on the prompt coherent radio emission model and emission predicted to occur when a neutron star collapses to form a black hole. At the putative host redshift of 1.8 for GRB 181123B, the non-detection of the prompt radio emission is two orders of magnitude lower than expected for magnetic reconnection models for prompt GRB emission and no magnetar emission is expected.

Key words: gamma-ray burst: individual: GRB 181123B – radio continuum: transients.

1 INTRODUCTION

The detection and association of the gravitational wave event, GW170817, and the short gamma-ray burst (SGRB) 170817A confirmed the theory that the progenitor of many SGRBs is the merger of two neutron stars (Abbott et al. 2017). However, the nature of the remnant formed via this merger is still debated, with the two competing models being a black hole or a massive, rapidly rotating, highly magnetized neutron star (hereafter referred to as a magnetar; e.g. Fong et al. 2016; Ai et al. 2018; Piro et al. 2019; Liu, Gao & Zhang 2020). Current gravitational wave observatories lack the sensitivity required to answer this question (e.g. Abbott et al. 2019), though the next generations of gravitational wave observatories may be able to measure the properties of the remnant in the future (e.g. Banagiri et al. 2020).

Tantalizing observational evidence shows that the central engine powering the GRB is active long after the merger of the two neutron stars, leading to flares and plateau phases in the electromagnetic light curve (Rowlinson et al. 2013). Rowlinson et al. (2013) showed that the plateau phases in X-ray light curves, following many SGRBs are consistent with the central engine being a magnetar. While support for this model has increased, there is currently no 'smoking gun' observation to prove that a magnetar was formed via the merger of two neutron stars. However, as outlined by Rowlinson & Anderson (2019) and references therein, if a magnetar is formed we would expect it to produce copious amounts of radio emission via a range of mechanisms. This radio emission is not expected if the remnant formed is a black hole. Identifying this radio emission would thus provide convincing support for the magnetar model.

Following the discovery of fast radio bursts (FRBs; e.g. Lorimer et al. 2007; Thornton et al. 2013), several of the progenitor theories suggested that they could come from cataclysmic events such as binary neutron star mergers (e.g. Zhang 2014). The discovery of repeating FRBs (such as FRB 121102; Spitler et al. 2014, 2016) showed that at least some FRBs were not coming from cataclysmic events. Therefore, either they are all not due to cataclysmic events or there are at least two different progenitors possible for FRBs. The recent detection of FRBs from the Galactic magentar SGR 1935+21 (The CHIME/FRB Collaboration et al. 2020; Kirsten et al. 2021) further supports the possibility of bright coherent radio emission coming from newborn magnetars formed during GRBs. Recent advances in the localization of FRBs within their host galaxies have revealed a variety of FRB host galaxy types and environments. Host

★ E-mail: b.a.rowlinson@uva.nl

galaxy comparison studies have found that a subset of the FRB hosts is consistent with the hosts of SGRBs (Margalit, Berger & Metzger 2019; Li & Zhang 2020). Gourdji et al. (2020) consider the likelihood that some of those non-repeating FRBs are consistent with some of the coherent radio emission models for compact binary mergers.

Previous efforts to identify this coherent radio emission following SGRBs have been unsuccessful. Early searches have either been very insensitive (>100 Jy) and/or have only sampled a small number of SGRBs to date (Cortiglioni et al. 1981; Inzani et al. 1982; Koranyi et al. 1995; Dessenne et al. 1996; Balsano et al. 1998). With the advent of the next generation of radio telescopes, with either large fields of view or rapid slew capabilities, searches have resumed in earnest to find this elusive emission. Recent searches using the Murchison Widefield Array (MWA; Tingay et al. 2013) and the Owens Valley Radio Observatory Long Wavelength Array (OVRO-LWA; Hallinan 2014) and the first station of the Long Wavelength Array (LWA1; Ellingson et al. 2013) have started obtaining constraining limits for SGRBs at low radio frequencies (for SGRBs 150424A, 170112A and 180805A; Obenberger et al. 2014; Kaplan et al. 2015; Anderson et al. 2018; Rowlinson & Anderson 2019; Anderson et al. 2021b). Meanwhile the LOw Frequency ARray (LOFAR; van Haarlem et al. 2013) has also demonstrated its potential to obtain deep constraints on this emission by following up the long GRB 180706A (Rowlinson et al. 2019). Additionally, at 1.4 GHz, the Australian Square Kilometer Array Pathfinder (ASKAP; Hotan et al. 2014) has followed up 20 GRBs (including four SGRBs) with their rapid response system (Bouwhuis et al. 2020). After searching their data for FRBs, they concluded there was no pulsed radio emission above 26 Jy ms. Although these are all non-detections to date, they have proven that the required sensitivities can be obtained to test the various models (Rowlinson & Anderson 2019). Many SGRBs do not show evidence of ongoing central engine activity and, hence, are more likely to have formed a black hole remnant so radio emission is not expected. Also, of the SGRBs with ongoing energy injection, these need to either be sufficiently energetic or nearby to produce detectable radio emission (Rowlinson & Anderson 2019).

Due to its sensitivity and rapid response mode enabling observations to start within 5 minutes of an alert, LOFAR is an ideal facility to chase the predicted radio emission. Since 2017, LOFAR has been responding fully automatically to GRB alerts and, on 2018 November 23, was successful in obtaining data following a SGRB detected by the Neil Gehrels Swift Observatory (hereafter referred to as *Swift*; Gehrels et al. 2004). This paper presents the deep search for coherent radio emission following this SGRB. In Section 2, we present the observational data obtained for this event, while in Section 3 we compare the observations to predictions tailored to this event.

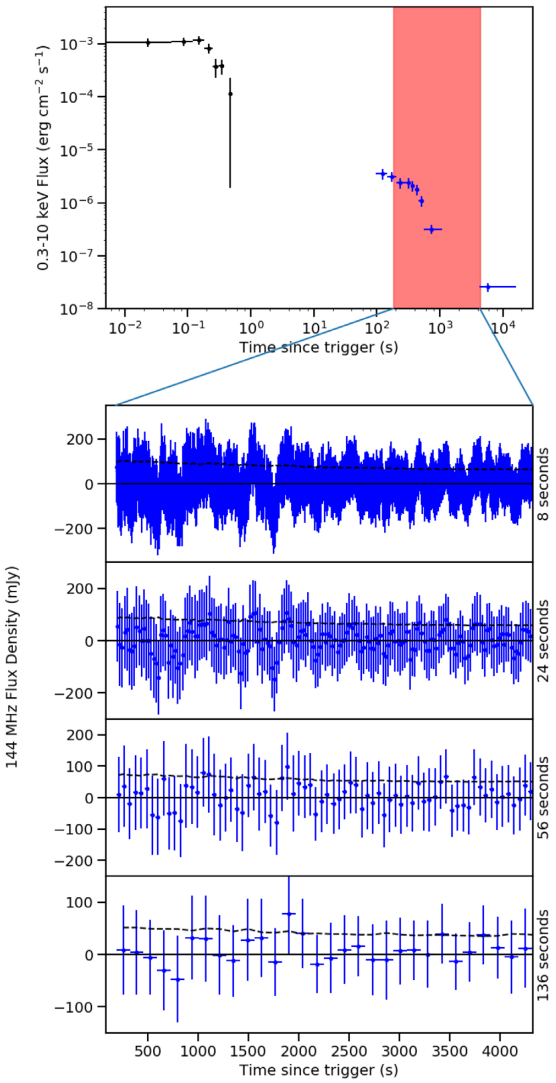

Figure 1. This figure, adapted from Rowlinson et al. (2019), shows the X-ray flux light curve of GRB 181123B in the 0.3–10 keV energy band (top panel) in which data from the BAT and XRT are shown with the black and blue data points, respectively. The time of the observation obtained by LOFAR is illustrated by the red-shaded region. The LOFAR 144 MHz flux density limits were measured at the position of GRB 181123B on four snapshot time-scales (8, 24, 56, and 136 s) and are illustrated in the bottom panel. We show the flux density of 0 Jy with a solid black line. The rms noise of each image is measured in the inner one-eighth of the image and is plotted with the dashed line.

2 OBSERVATIONS OF GRB 181123B

2.1 Swift observations

The *Swift* Burst Alert Telescope (BAT; Barthelmy et al. 2005) triggered and located GRB 181123B (trigger = 873186) on 2018 November 23 at 05:33:03 UT (Lien, D'Avanzo & Palmer 2018). *Swift* slewed immediately to the burst, and X-Ray Telescope (XRT; Burrows et al. 2005) observations began 80.2 s after the BAT trigger, locating the X-ray afterglow to within a 90 per cent error region of 1.6 arcsec radius at a position of RA: 184.36686 degrees, Dec: 14.59788 deg.[1] The duration of $T_{90} = 0.4$ s (Lien et al. 2018) and the lag analysis (Norris, Barthelmy & Lien 2018) confirm that this is a short GRB, possibly accompanied by extended emission (observed at low significance). The GRB was also detected above the BAT energy band by Insight-HXMT, which recorded a duration of 0.23 s (Yi et al. 2018). *Swift's* UltraViolet and Optical Telescope (UVOT; Roming et al. 2005) did not detect a counterpart (Oates & Lien 2018).

In Fig. 1, we show the *Swift* BAT and XRT 0.3–10 keV observed flux light curves (black and blue data points respectively) obtained using the *Swift* Burst Analyser (Evans et al. 2010). The light curve consists of a single prompt, γ-ray flare followed by a fading X-ray counterpart that is modelled using a single power-law decline of $\alpha_X = 1.31^{+0.15}_{-0.14}$ (Burrows et al. 2018).

[1] www.swift.ac.uk/xrt_positions

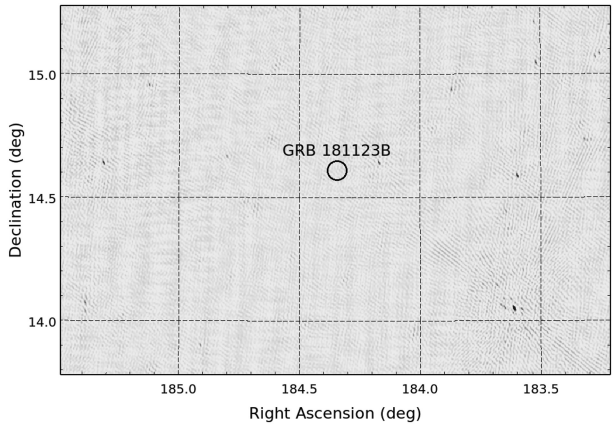

Figure 2. This image of the region surrounding GRB 181123B was attained using 71.2 min of LOFAR data. The circle shows the location of GRB 181123B and the 3σ upper limit on the flux density of this event is 60 mJy beam^{-1}.

2.2 Other observations

A faint and likely extended near-infrared counterpart within the XRT error circle was reported 9.2 h after the trigger with $i(AB) \sim 23.32 \pm 0.25$ (Fong, Tanvir & Levan 2018) and $J(AB) \sim 22.94 \pm 0.19$ (Paterson & Fong 2018). A second observation of that source found a marginal detection with $J(AB) > 23.3$ (Paterson et al. 2018) at 3.38 d. Following further analysis, this source is identified as the putative host galaxy of GRB 181123B at a redshift of $z = 1.8$ with a chance alignment probability of $\lesssim$0.44 per cent (Paterson et al. 2020). We note that only one emission line was detected in the optical spectrum. This emission line is attributed to H β resulting in the redshift being 1.8, which is consistent with the photometric constraints (Paterson et al. 2020).

An 8.3 h radio observation was also obtained using the Australia Telescope Compact Array rapid-response mode, which automatically triggered observations when the source was above the horizon, starting at 12.6 h post-burst and providing 3σ upper limits of 34 and 32 microJy beam^{-1}, respectively (Anderson et al. 2021b).

2.3 LOFAR observations

Since November 2017, LOFAR has been able to fully automatically respond to transient alerts, which are typically communicated via VOEvents (Williams & Seaman 2006). We utilize VOEvents that are redistributed via the 4 PI SKY BROKER (Staley & Fender 2016) and receive them using the COMET broker software (Swinbank 2014). Transients are then filtered according to predetermined triggering criteria, including identification of source (GRB), *Swift* trigger integration time ($\leq$1 s), elevation of the source ($\geq$15 deg), and calibrator availability. Following this, an XML observing request is sent to the LOFAR system. GRB 181123B passed the triggering criteria and LOFAR observations started 4.4 min after the GRB occurred. A 2 h LOFAR observation was started at 05:37:25 UTC on 2018 November 23 and was centred on the BAT localization of GRB 181123B. The observation time is highlighted by the red shaded region in Fig. 1. Unfortunately, due to a scheduling error, the full observation was not completed (total usable observation time attained: 71.2 min) and the calibrator observation was not completed automatically. The LOFAR Radio Observatory manually scheduled a 15 min calibrator observation of 3C 286 at 13:20:03 UTC on 2018 November 23.

In order to benefit from the deep 8 h images attained for much of the Northern hemisphere by the LOFAR Two Meter Sky Survey (LoTSS; Shimwell et al. 2019), we matched our observational set-up to that of LoTSS. When available, the LoTSS observations provide a deep comparison image and accurate sky model of the field for calibration purposes. For these observations, we used the LOFAR High Band Antennas (HBA) with a central frequency of 144 MHz. The frequency range is 120–168 MHz, covered by 244 sub-bands each with a bandwidth of 195.3 kHz. We used the Dutch LOFAR stations, 23 core stations and 11 remote stations. The data were recorded using a time-step of 1 s and 64 channels per sub-band. Our observations were pre-processed using the standard methods for LOFAR (van Haarlem et al. 2013).

2.3.1 *Calibration*

Following the method outlined in Rowlinson et al. (2019), the LOFAR observations were calibrated using PREFACTOR[2] and a strategy based upon that presented in van Weeren et al. (2016). Both the target and calibrator observations were flagged for excess radio frequency interference using AOFLAGGER (Offringa et al. 2010; Offringa, van de Gronde & Roerdink 2012). One of the brightest sources in the radio sky, Virgo A, is 3.9 deg from the position of the GRB and dominated the radio image. Using the detailed skymodel provided with PREFACTOR, we removed the contribution of Virgo A from the observations. The calibrator and target visibility data were averaged in time to 8 s and in frequency to 48.82 kHz (4 channels per subband).

Using the model obtained by Scaife & Heald (2012), we obtained the diagonal gain solutions for the calibrator source 3C 286, which were then transferred to the target visibility data. The target subbands were combined in groups of 10, resulting in combined data sets of 1.953 MHz. A sky model of the target field was obtained using the global sky model developed by Scheers (2011) and the TIFR GMRT Sky Survey at 150 MHz (TGSS; Intema et al. 2017).[3] The sky model of the field was then used to conduct a phase calibration of the target visibilities.

2.3.2 *Imaging*

We imaged the full LOFAR observation using WSCLEAN (Offringa et al. 2014) using a primary beam correction, Briggs weighting (robustness of -0.5), a pixel scale of 10 arcsec, and baselines up to 12 km. Cleaning was conducted using an automatic threshold and 10^4 iterations. The final image has a central frequency of 144 MHz and a bandwidth of 48 MHz. The image has a typical angular resolution of $\sim$30 arcsec. The region surrounding GRB 181123B is shown in Fig. 2 and the image rms at the GRB location (30 arcsec radius) is 20 mJy beam^{-1}, corresponding to a 3σ upper limit of 60 mJy beam^{-1}. Using the Python Source Extractor (PYSE; Carbone et al. 2018), we also conduct a forced source extraction at the position of the GRB holding the shape and size of the Gaussian shape fitted fixed to the restoring beam shape. We measure a peak flux density of -29 ± 38 mJy beam^{-1} (the uncertainty on this value is as measured by PYSE; Carbone et al. 2018).

We created a Stokes I image of the visibilities using WSCLEAN (Offringa et al. 2014)[4] with Briggs weighting, a pixel scale of 10 arcsec and baselines up to 12 km. As the image integration times

[2] https://github.com/lofar-astron/prefactor
[3] http://tgssadr.strw.leidenuniv.nl/doku.php
[4] http://wsclean.sourceforge.net

Table 1. Here, we provide the average rms noise and its 1σ standard deviation for each set of images from the four time-scales considered.

Time-scale (s)	rms noise (mJy beam^{-1})
8	76 ± 12
24	69 ± 9
56	58 ± 8
138	42 ± 5

increased, we found that the automatic CLEAN process in WSClean was diverging, likely due to remaining noise contributions following the subtraction of Virgo A and confusion noise, so the CLEAN process was stopped after 10 000 iterations. Therefore, the typical rms noise is not expected to follow the expected relationship that the rms noise drops as $t^{\frac{1}{2}}$, where t is the integration time.

As the X-ray data may show a plateau phase out to ∼400 s, we first created a radio image using the first 136 s of data to search for emission associated with this phase. The image rms at the GRB location (30 arcsec radius) is 51 mJy beam^{-1}, corresponding to a 3σ upper limit of 153 mJy beam^{-1}. At the putative host galaxy redshift of 1.8, this corresponds to a luminosity of 2.5×10^{44} erg s^{-1}. Using PYSE, we measure a peak flux density of -9 ± 50 mJy beam^{-1}, corresponding to a non-detection. Additionally, using the intervals-out option in WSCLEAN, we created snapshot images using the source-subtracted visibilities of durations 8, 24, 56, 136 s (the motivation for this range of time-scales is outlined in Section 3.3).

We use the monitoring list capability of the LOFAR Transients Pipeline (TRAP; Swinbank et al. 2015) to measure the flux density at the location of the GRB. TRAP also monitors the typical rms noise in the inner one-eighth of the input images. In Table 1, we give the typical rms noise for the different imaging time-scales.

The light curves were obtained from TRAP for each of the four time-scales used and are plotted as the blue data points in Fig. 1. We show the image rms using the black dashed line and it can be seen that GRB flux densities are consistent with the image rms noise (note, when the local rms is lower than the image rms, the blue data points can lie below the black dashed lines). Therefore, no coherent emission was detected from GRB 181123B in this analysis.

3 MODELLING AND INTERPRETATION

In the following analysis, we need to utilize the rest-frame properties of GRB 181123B in order to compare our observations to the various models predicting coherent radio emission. As outlined in Section 2.2, there is a host galaxy candidate at a redshift of $z \sim 1.8$ with a very low probability of chance alignment and we consider the implications of this on each model. However, as the redshift is not from a direct measurement of the afterglow and hence still has the possibility of being a chance association, we also treat the redshift as unknown in the following analysis. In Section 3.2, we calculate the minimum redshift ($z \sim 1.05$) above which the prompt radio emission can be probed by our LOFAR observations assuming dispersion effects. In Section 3.4, we use an average SGRB redshift of 0.7 to fit the magnetar model (consistent with analysis in Rowlinson et al. 2013; Rowlinson & Anderson 2019; Rowlinson et al. 2019; Anderson et al. 2021a) and then analytically scale the results to a range of redshifts.

3.1 Propagation effects for low-frequency radio emission

Coherent radio emission is known to be subject to significant propagation affects, limiting its ability to be detectable at low radio frequencies. Plasma close to the source is opaque below a fixed frequency that is directly proportional to the number density of electrons in the plasma, thus dense regions may be able to block coherent radio emission at LOFAR frequencies. Zhang (2014) showed that in the case of SGRBs, such as GRB 181123B, the emission is expected to be able to escape along the jet propagation axis.

Additionally, the surrounding medium can interact with the low-frequency photons, leading to free–free absorption, with a strong dependence on the temperature and density of the surrounding interstellar or intergalactic medium. Using the X-ray spectrum of GRB 181123B, we are able to estimate the absorption due to neutral hydrogen along the line of sight to this GRB. Using the automated X-ray spectrum provided by the UK *Swift* Science Data Centre, GRB 181123B has an intrinsic absorption column of $N_H = 2.5^{+6.6}_{-2.5} \times 10^{20}$ cm^{-2}. This is a low-absorption column, consistent with zero intrinsic absorption, showing that GRB 181123B most likely occurred in a very low-density medium so free–free absorption is expected to be low.

These propagation affects are considered in depth by Rowlinson & Anderson (2019), who show that they are likely to not affect the coherent radio emission in compact binary mergers such as the likely progenitor of GRB 181123B.

3.2 Constraints on prompt emission

We are able to place constraints on the presence of prompt radio emission from GRB 181123B even though the LOFAR observations do not cover the same time period as the prompt gamma-ray emission. This is because it takes longer for radio emission to propagate to the Earth than it does for the gamma-ray emission. This is due to dispersion delay, a frequency-dependent delay due to the integrated column density of free electrons along the line of sight. The dispersion delay, τ, in seconds is given by

$$\tau = \frac{\mathrm{DM}}{241\nu^2_{\mathrm{GHz}}} s, \quad (1)$$

where DM is the dispersion measure in pc cm^{-3} and ν_{GHz} is the observing frequency in GHz (Taylor, Manchester & Lyne 1993). Given the 4.4 min delay between the prompt emission and the start of the LOFAR observations, we are able to probe DM values $\geq$1319 pc cm^{-3}. According to the NE20001 model of free electrons in our Galaxy, the Galactic component of the DM in the line of sight towards GRB 181123B is 56 pc cm^{-3} (Cordes & Lazio 2002). Assuming a relation between DM and redshift ($DM \sim 1200z$ pc cm^{-3}; e.g. Ioka 2003), we are able to constrain the prompt emission for redshifts $\gtrsim 1.05$ (assuming zero contribution from their host galaxy and subtracting the contribution of 56 pc cm^{-3} from the Milky Way).

If the prompt coherent radio emission originates from the same location as the prompt gamma-ray emission, we can constrain the power ratio, $\langle\delta\rangle$:

$$\langle\delta\rangle = \frac{\Phi_r}{\Phi_\gamma}, \quad (2)$$

where Φ_r and Φ_γ are the radio and gamma-ray bolometric fluences, respectively. The model proposed by Usov & Katz (2000), in which the radio and gamma-ray emission originate from magnetic

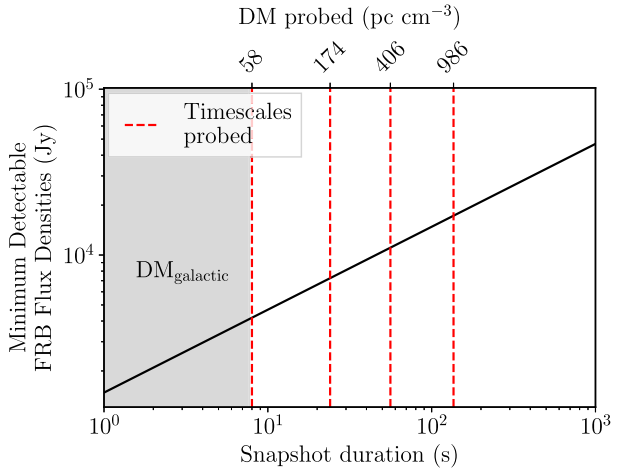

Figure 3. The minimum FRB flux density detectable in the LOFAR observations of GRB 181123B. Here, we assume that the dispersed signal duration across the frequency band is equal to the snapshot duration. The snapshot durations used in this analysis are shown by the red dashed lines, with their corresponding DM values shown on the top *x*-axis. The shaded region illustrates the Galactic component of the DM in the sight line towards GRB 181123B.

reconnection in a strongly magnetized jet, can be constrained using this ratio and it is equivalent to $\langle\delta\rangle \simeq 0.1\epsilon_B$ where ϵ_B is the proportion of energy contained in the magnetic fields. In Rowlinson et al. (2019), we show for typical GRB gamma-ray spectra and observations at 144 MHz that

$$\langle\delta\rangle \simeq [4.7-7.2]\times10^9(1+z)^{0.6}\epsilon_B^{-0.3}\frac{\Phi_\nu}{\Phi_\gamma}, \quad (3)$$

where Φ_ν is the fluence limit obtained in the shortest snapshot radio images, corresponding to a 3σ limit of 1.8 ± 0.3 Jy s for our 8 s images for GRB 181123B (see Table 1). The gamma-ray fluence for GRB 181123B was measured by *Swift* to be $3.8\pm1.2\times10^{-7}$ erg cm^{-2} in the 15–350 keV energy band (Palmer et al. 2018). As stated in Section 2.2, the potential redshift of this GRB is $z=1.8$. Thus, we can constrain the fraction of energy stored in the magnetic fields within the relativistic jets of GRB 181123B to be $3\times10^{-5}\lesssim\epsilon_B\lesssim2\times10^{-4}$ (uncertainties in observed values have been propagated and are included in this range). Therefore, we are able to rule out this model as ϵ_B is at least two orders of magnitude lower than expected for magnetic re-connection models for the prompt emission in GRBs (e.g. Beniamini & Piran 2014).

Therefore, future observations of high-redshift events or with a more rapid slew time would enable us to tightly constrain the Usov & Katz (2000) model (see also the application of this model to LOFAR follow-up of X-ray flares by Starling et al. 2020).

3.3 Constraints on FRBs

As outlined in the introduction, a proportion of the FRBs may be associated with the merger of two neutron stars, with the emission originating from mechanisms prior to the merger, during the merger or post-merger (see e.g. Rowlinson & Anderson 2019; Gourdji et al. 2020; and references therein). The LOFAR observation of GRB 181123B can be utilized to constrain the emission from dispersed FRBs originating from this source.

Here, we use the method outlined in Rowlinson et al. (2019) to determine the optimal snapshot time and the associated minimum detectable FRB flux densities at a range of dispersion measures (DMs). For consistency with previous works, the width of an FRB is assumed to be 1 ms. The minimum detectable flux densities are obtained using equations (2) and (3) in Rowlinson et al. (2019), scaled using the 3σ upper limit of 126 mJy obtained in the 138 s integrated images. As the rms noise values are not following the typical relationship of $t^{\frac{1}{2}}$ (see Section 2.3.2), this provides conservative minimum detectable flux densities. The optimal snapshot time, for the LOFAR observing band of 120.5–167 MHz, for a given DM value is calculated using equation (4) in Rowlinson et al. (2019). We assume this GRB occurred within a redshift of 1, corresponding to an IGM contribution to the DM of up to 1000 pc cm^{-3} with a Galactic contribution of 56 pc cm^{-3} (including a contribution of 30 pc cm^{-3} from our Galaxy halo; Yamasaki & Totani 2020; Dolag et al. 2015). Then, using a minimum snapshot integration time of 8 s, we use 4 snapshot timescales roughly logarithmically spaced to cover this range of 8, 24, 56, and 136 s. The minimum detectable FRB flux densities as a function of the snapshot time-scale, or DM, are plotted in Fig. 3. In the 8 s snapshot images, we are sensitive to FRBs with flux densities $\gtrsim$400 Jy. No FRBs were detected in the snapshot images of GRB 181123B.

3.4 Constraints on the magnetar central engine model

As outlined in Section 1, SGRBs like GRB 181123B are believed to originate from the merger of two neutron stars or a neutron star and a black hole. A number of theories have been proposed to produce coherent radio emission between stages prior to and following the merger process (see Rowlinson et al. 2019; Gourdji et al. 2020; and references therein). SGRBs exhibiting a plateau phase in their X-ray light curves are consistent with mergers of two neutron stars that combine to form a hypermassive neutron star with high magnetic fields (hereafter referred to as magnetars; Rowlinson et al. 2010, 2013). If the X-ray plateau phase is followed by a steep decay phase, these are interpreted to be magnetars that are too massive to become stable neutron stars and collapse to form a black hole. As can be seen in Fig. 1, the X-ray light curve of GRB 181123B shows a plateau phase and a subsequent steep decay phase. Thus, GRB 181123B can be explained as a merger of two neutron stars that led to an unstable magnetar that collapsed a few hundred seconds after its formation. Therefore, in this section, we are able to test two of the models outlined by Rowlinson & Anderson (2019) relating to the formation and subsequent collapse of a magnetar.

3.4.1 Modelling of X-ray light curve

Assuming a magnetar was produced during GRB 181123B and is powering the plateau phase in the X-ray light curve, we can deduce the key magnetar parameters by fitting the magnetar model to the rest-frame light curve. Following the method outlined in Rowlinson et al. (2013) and Rowlinson et al. (2019), we take the observer frame X-ray light curve (as shown in Fig. 1) and convert it to a rest-frame light curve in the 1–10 000 keV energy band. In this conversion, we assume the average SGRB redshift of 0.7 (e.g. Rowlinson et al. 2013) and use a *k*-correction (Bloom, Frail & Sari 2001).

Using the method outlined in Rowlinson et al. (2013, 2019), we fitted the magnetar model (Zhang & Mészáros 2001) to the rest-frame light curve. In the subsequent analysis, we utilize $f\sim3.45$ (where f is a factor encompassing the beaming angle and efficiency uncertainties), following the analysis of Rowlinson et al. (2019).

We find that the rest-frame light curve, at a redshift of 0.7, can be fitted with an unstable 1.4 M$_\odot$ magnetar that collapses at ∼400 s with

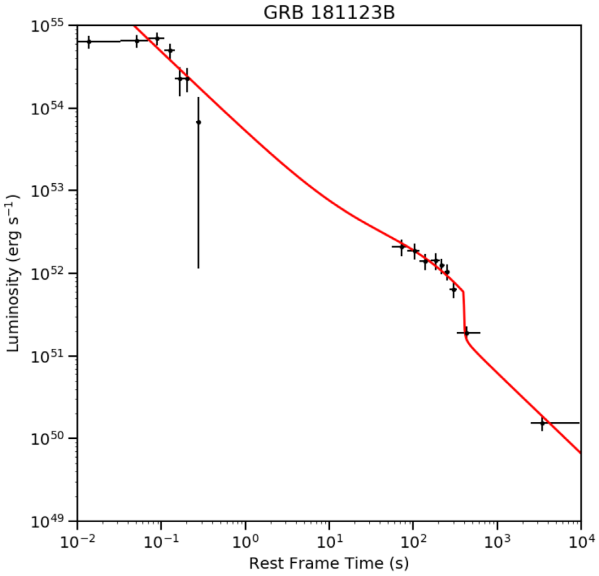

Figure 4. This figure shows the rest-frame X-ray light curve, assuming a redshift of 0.7. The red line shows the magnetar model fit obtained, corresponding to a magnetic field of $2.4^{+1.3}_{-1.3} \times 10^{14}$ G and spin period of $0.095^{+0.011}_{-0.020}$ ms.

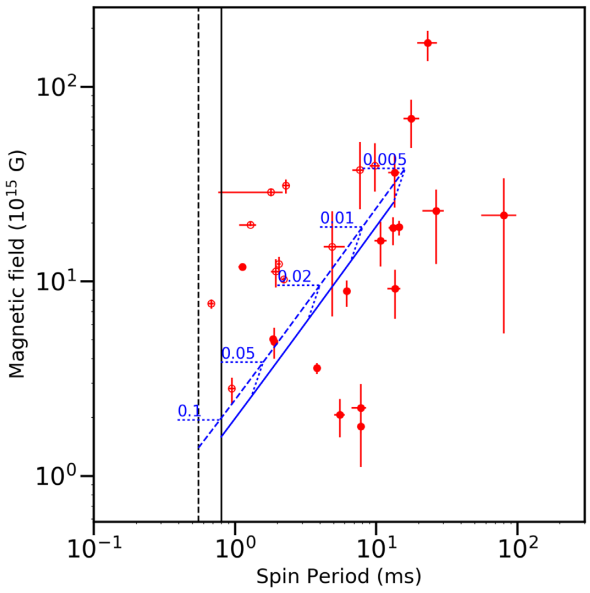

Figure 5. This figure shows the magnetic fields and spin periods for the population of SGRBs fitted with the magnetar model (red data points from Rowlinson et al. 2013). The black vertical lines represent the spin break-up periods for 1.4 $M_\odot$ (solid line) and 2.1 $M_\odot$ (dashed line) neutron stars. The blue diagonal lines show the solutions for GRB 181123B (1.4 $M_\odot$ with a solid line and 2.1 $M_\odot$ with a dashed line) at a range of redshifts (some labelled for reference) up to the spin break-up limits. GRB 181123B would need to be at a redshift <0.08 to be consistent with forming a 1.4 $M_\odot$ magnetar or at a redshift <0.14 to be consistent with forming a 2.1 $M_\odot$ magnetar.

a magnetic field of $2.4^{+1.3}_{-1.3} \times 10^{14}$ G and spin period of $0.095^{+0.011}_{-0.020}$ ms [note Sarin, Lasky & Ashton (2020) also modelled this GRB using a Bayes inference fitting technique and found an earlier collapse time of 250 s]. In addition to the magnetar component, there is a power-law decay from the prompt gamma-ray emission, with a slope of $\alpha = 0.973^{+0.039}_{-0.040}$. We show this fitted model in Fig. 4.

For the assumed redshift of 0.7, we find that the fitted magnetar is spinning unphysically fast as it is spinning significantly faster than the spin break-up limit (0.8 ms for a 1.4 $M_\odot$ neutron star; Lattimer & Prakash 2004). For a higher mass neutron star of 2.1 $M_\odot$, as might be expected from a neutron star merger, the spin break-up limit is a lower value (0.55 ms, as calculated using equation 3 of Lattimer & Prakash 2004, assuming a radius of 10 km). For an unstable 2.1 $M_\odot$ magnetar, we find a magnetic field of $3.6^{+2.0}_{-1.9} \times 10^{14}$ G and spin period of $0.116^{+0.017}_{-0.024}$ ms. However, the fitted spin period at a redshift of 0.7 for this heavier magnetar scenario is still significantly smaller than the 0.55 ms spin break-up period. Therefore, if GRB 181123B is to be explained using the magnetar central engine model, the redshift of the event must be significantly lower than the average SGRB redshift. We can thus constrain the redshift of GRB 181123B by assuming that a magnetar, with spin period less than the spin break-up, was formed. Using the following scalings (from Rowlinson & Anderson 2019; Rowlinson et al. 2019), we can determine the magnetic fields and spin periods as a function of the assumed redshift,

$$B \propto \frac{(1+z)}{D_L}, \tag{4}$$

$$P \propto \frac{(1+z)^{\frac{1}{2}}}{D_L}, \tag{5}$$

where B is the magnetic field of the magnetar and P is the initial spin period of the magnetar.

In Fig. 5, we plot the magnetic field and spin period of GRB 181123B, for a range of redshifts from z = 0.005 up to the highest redshift attainable before the spin period is faster than that allowed by the spin break-up limit. We plot the solutions for both a 1.4 $M_\odot$ (solid blue line) and a 2.1 $M_\odot$ (dashed blue line) neutron star.

For comparison, we also show the population of SGRBs fitted by the magnetar model from Rowlinson et al. (2013). We find the maximum redshifts that GRB 181123B could have occurred at (and still be fitted with the magnetar model) are $z_{\rm max} = 0.08$ and $z_{\rm max} = 0.14$, for the 1.4 $M_\odot$ and 2.1 $M_\odot$ scenarios, respectively. As the fitted model shows that the magnetar collapsed at ∼400 s, the observations are consistent with a higher mass magnetar being formed. We note that at the putative host redshift of this event, $z = 1.8$, it is impossible to form a magnetar as this model predicts a spin period significantly faster than the spin break-up limit.

3.4.2 Host galaxy constraints

As noted in Section 2.2, a likely host galaxy was observed at a redshift of 1.8 with a probability of chance alignment of 0.44 per cent (Paterson et al. 2020). As this host identification has a small, but non-negligible, probability of being a chance alignment, we also consider other host galaxy candidates for GRB 181123B. Since compact binary systems can be found at significant offsets from their hosts, due to natal kicks or dynamical processes (e.g. Salvaterra et al. 2010; Tunnicliffe et al. 2014; Bray & Eldridge 2016), we performed a catalogue search beyond the XRT error circle. To take the nearest in separation, we briefly discuss galaxies of interest within 20 arcsec of the UVOT-enhanced XRT position. We find one galaxy with redshift only just beyond the $z = 0.14$ limit for a magnetar engine following our X-ray analysis in Section 3.4.1. SDSS J121727.68+143609.2 has a photometric redshift estimate of 0.326 ± 0.101 (e.g. Alam et al. 2015) and can be classified as an early-type galaxy when considering the SDSS *ugr* colours (Strateva et al. 2001). At that redshift and with a separation from the XRT position of 17.6 arcsec, the implied projected offset is

84 kpc. Two further SDSS galaxies are found at smaller separations of ∼7 arcsec: SDSS J121728.29 + 143546.3 at $z = 0.575 \pm 0.043$ and impact parameter 51 kpc, classified as a red, early-type galaxy and SDSS J121728.29+143546.4 (WISEA J121728.29+143546.2) which has no redshift but can be classified as a starburst galaxy from its *WISE* colours, consistent with a late-type classification from the SDSS colours.

We then carried out a catalogue search using NED and SIMBAD, for all galaxies with known distance ≤366 Mpc (corresponding to our X-ray limit of $z \leq 0.08$ for a 1.4 $M_\odot$ magnetar) and projected offset ≤200 kpc, using the galaxy-matching method of Mandhai et al. (2019). This results in five galaxy candidates. Three are 2MASX sources associated with bright galaxies NGC 4254, NGC 4262, and IC 3065 at distances 13.9–16.6 Mpc and with impact parameters spanning 91–164 kpc. These galaxies have significant separations from the GRB, however, of 22–34 arcmin. Two are faint galaxies in SDSS-DR12, found at 7 and 2 arcmin separations, respectively: SDSS J121753.41+143228.2, at 76 Mpc distance with impact parameter 156 kpc, which can be classified as an early-type galaxy and SDSS J121721.17 + 143706.6, at 285 Mpc and impact parameter 170 kpc, with a *WISE* counterpart and classified as a late-type galaxy. These are therefore promising host candidates.

3.4.3 Pulsar-like emission

Assuming a 2.1 $M_\odot$ magnetar was formed, we can predict the expected pulsar emission from this source assuming the model proposed by Totani (2013, see also Pshirkov & Postnov 2010) following the method outlined in Rowlinson et al. (2019). The predictions made in the following section only change slightly for the 1.4 $M_\odot$ magnetar and hence the conclusions drawn hold even if the magnetar has a lower mass. Totani (2013) showed that the radio flux density of the pulsar like emission produced by the newly formed magnetar is given by

$$F_\nu \simeq 8 \times 10^7 \nu_{\rm obs}^{-1} \epsilon_r D_{\rm lum}^{-2} B_{15}^2 R_6^6 P_{-3}^{-4} \ {\rm Jy}, \quad (6)$$

where $D_{\rm lum}$ is the luminosity distance in Gpc, $\nu_{\rm obs}$ is the frequency in MHz, $R = 10^6 R_6$ cm is the radius of the magnetar and ϵ_r is the efficiency. In this model, we assume that the pulsar magnetic field axis is directed towards Earth (see the discussion in Rowlinson, Patruno & O'Brien 2017) and that the magnetar is emitting via dipole radiation (see Lasky et al. 2017 for further discussion). In this analysis, we take the typical pulsar efficiency of 10^{-4} (e.g. Taylor et al. 1993) but note that this value is poorly known (see Rowlinson & Anderson 2019; Rowlinson et al. 2019 for further discussion). Taking into account the uncertain parameters in the models, namely f and ϵ_r, we find that the predicted flux density is given by

$$F_\nu = 6.8^{+38}_{-5.9} \times 10^7 \ \frac{\epsilon_r}{f} \ {\rm Jy}. \quad (7)$$

The fraction f can be constrained to be 3.45 ± 0.29 (Rowlinson et al. 2014; Rowlinson & Anderson 2019). Therefore, given the predicted value of F_ν, the allowed range of f, and the observed LOFAR upper limit of the flux density at the position of GRB 181123B in the 400 s integrated observation of 153 mJy, we find that $\epsilon_r \leq 6 \times 10^{-8}$. Therefore, as no emission was detected, it is shown that GRB 181123B either did not form a magnetar (consistent with the expectation if associated with the candidate host galaxy at $z = 1.8$), the surrounding medium is effectively blocking the emission, the beaming of the radio emission is different to that of the X-ray emission or the model proposed by Totani (2013) is not correct. In Anderson et al. (2021b), they consider the same model for the short GRB 180805A; however for that event the emission was predicted to be too faint to be observable due to having a lower energy magnetar (from fitting the X-ray light curve its spin was slower and the magnetic field was lower than that fitted for GRB 181123B). More observations of other GRBs will be required to increase the statistical significance of this non-detection and to explore the observed range of magnetic fields and spin periods.

3.4.4 Emission associated with collapse to black hole

Assuming a magnetar was formed during SGRB 181123B, the X-ray fitting suggests it was an unstable neutron star that collapsed to form a black hole at ∼400 s abruptly ending the plateau phase (see Section 3.4.1). This collapse is thought to be accompanied by a brief flash of coherent radio emission as magnetic reconnection occurs within the pulsar magnetosphere (Falcke & Rezzolla 2014; Zhang 2014). As shown in Rowlinson et al. (2019), the observed flux density, f, at a given observing frequency, $\nu_{\rm obs}$, can be described as

$$f_\nu = -\frac{10^{-23} \epsilon E_{\rm B}}{4\pi D_{\rm lum}^2 \tau} (\alpha + 1) \nu_p^{-(\alpha+1)} \frac{\nu_{\rm obs}^\alpha}{(1+z)} \frac{\tau}{t_{\rm int}} \ {\rm Jy}, \quad (8)$$

where $E_{\rm B}$ is the amount of energy available in the magnetic field of the neutron star in erg (given by $E_b = 1.7 \times 10^{47} B_{15}^2 R_6^3$ erg), ϵ is the fraction expected to be converted into coherent radio emission, $t_{\rm int}$ is the intrinsic duration of the emission in seconds (assumed to be 1 ms in this analysis; Falcke & Rezzolla 2014), α is the spectral index of the radio emission, $\nu_{\rm p}$ is the plasma frequency given by $\nu_{\rm p} \simeq 9 n_{\rm e}$ kHz, $n_{\rm e}$ is the number density of electrons in cm^{-3} and $t_{\rm int}$ is the integration time of the image in seconds.

For GRB 181123B, we assume a spectral slope of the coherent radio emission to be $\alpha = -2$, the efficiency to be $\epsilon = 10^{-6}$ and take the magnetar parameters from Section 3.4.1. In Fig. 6, we plot the predicted fluence for this event (with the upper and lower bounds being for $\epsilon = 10^{-4}$ and 10^{-8}, respectively) and over plot the fluence limit attained in our shortest snapshot images (a flux limit of 76 mJy in an 8 s image corresponds to 1.8×10^3 Jy ms). From this analysis, we would only have a chance of detecting this emission if GRB 181123B occurred at a redshift ≲0.05 and the efficiency is of order 10^{-4}. We note that if the assumed spectral index was larger than $\alpha = -2$, this emission would be easily detectable by our LOFAR observations.

Our non-detection can be interpreted in a number of ways. First, the efficiency and spectral index of the emission is low and hence it is undetectable in our images. Making shorter duration images and/or conducting image plane de-dispersion (as in Anderson et al. 2021b) will increase the chance of detection. Secondly, the merger was expected to be at a higher redshift than 0.05 and hence too distant to be detected. Thirdly, the interpretation that the X-ray light curve shows the formation and collapse of a magnetar is incorrect. Fourthly, the emission is beamed away from us or is unable to propagate through the surrounding medium. As found in Section 3.4.3, more observations of other GRBs are required to determine which is the most likely interpretation for this non-detection.

4 CONCLUSIONS

In this study, we have found no evidence for low frequency, coherent radio emission originating from SGRB 181123B. We searched for persistent emission during the plateau phase and short duration radio flares throughout the full observation. We have compared this non-detection to theoretical models to place deep and constraining

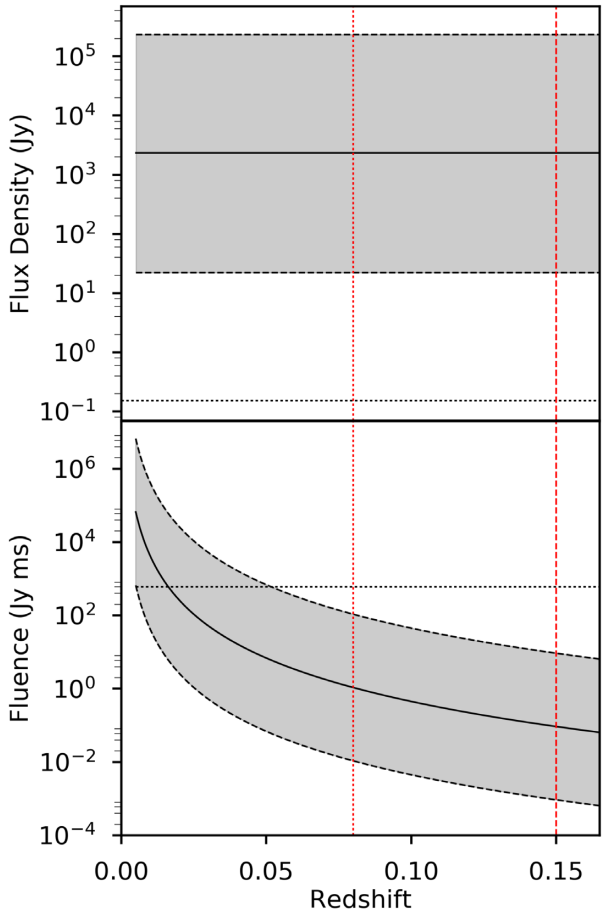

Figure 6. In this figure, we show the predicted emission as a function of redshift for the two coherent emission models considered for GRB 181123B (black solid lines) with their associated 1σ uncertainties (black dashed lines and shaded region). The red dotted vertical lines show the maximum redshifts of 0.08 and 0.14, for a 1.4 $M_\odot$ magnetar and a 2.1 $M_\odot$ magnetar, respectively. Top: This shows the predicted flux density for a spinning down magnetar (c.f. Section 3.4.3), assuming a pulsar efficiency of $\epsilon = 10^{-4}$. The observed 3σ flux density limit of 153 mJy during the plateau phase is shown as the black dotted horizontal line. Bottom: This shows the predicted fluence for a magnetar collapsing to form a black hole (c.f. Section 3.4.4), assuming an efficiency of 10^{-6} with the shaded area representing an efficiency range of 10^{-4}–10^{-8}. The observed 3σ fluence limit of 1.8×10^3 Jy ms for the 8 s images is shown as the black dotted horizontal line.

limits. Assuming the putative host galaxy redshift, we are able to rule out theoretical models as outlined below. As there is still some uncertainty given the possibility of a chance alignment with that galaxy, we also draw conclusions assuming that the redshift is unknown.

Assuming that GRB 181123B was at a redshift greater than 1.05, we are able to show that our non-detection implies that the fraction of energy contained within the magnetic fields in the relativistic jets is an order of magnitude lower than expected for magnetic reconnection models for GRB prompt emission. This limit decreases to being two orders of magnitude lower than the models for the case of the redshift of the likely host galaxy. More rapid slew times for radio telescopes are required to be able to constrain this model for lower redshifts. Starling et al. (2020) also aims to constrain this model at low redshift for X-ray flares, which are believed to be from the same emission mechanism as the prompt gamma-ray emission, by exploiting the observed delay between triggering on the prompt emission and the X-ray flares enabling simultaneous radio observations.

The X-ray light curve of GRB 181123B shows evidence of ongoing energy injection during the first few hundred seconds before stopping abruptly and resuming a power-law decay associated with the afterglow phase. We interpret this energy injection as resulting from a newborn magnetar, formed via the merger of two neutron stars, which collapses to form a black hole at ∼400 s. By fitting the X-ray light curve, we were able to constrain the magnetar parameters required to test coherent radio emission models. We find that the magnetar parameters are unphysical for redshifts >0.14 for a 2.1 $M_\odot$ neutron star (>0.08 for a 1.4 $M_\odot$ neutron star). Thus, if this model is correct, we would expect the event to occur at a low redshift. We find there are catalogued galaxies that would be consistent with this interpretation, all offset from the GRB localization implying significant kicks. However, at the proposed redshift of the likely host galaxy, this model and its associated coherent radio emission is ruled out.

The first model tested was that of pulsar like emission from the newly formed magnetar during the energy injection phase (e.g. Totani 2013). We find that the predicted emission is ∼4 orders of magnitude brighter than the upper limited obtained assuming an efficiency of 10^{-4} expected for standard pulsars. We can constrain the efficiency of conversion of rotational energy into coherent radio emission for the newborn neutron star to be $\leq 6 \times 10^{-8}$. Explanations for this non-detection that require further study include absorption of the emission by the surrounding medium or the beaming of the X-ray emission is different to that of the radio emission.

The second model tested predicted a short flash of coherent radio emission when the magnetar collapses to form a black hole and magnetic reconnection of the field lines occurs (Falcke & Rezzolla 2014; Zhang 2014). We find this emission would only be detectable for events at redshifts ≤0.05 for an assumed efficiency of 10^{-6} and a radio spectral index of −2. Therefore, our non-detection is consistent with this model.

Analysis of GRB 181123B shows the ability of the current generation of radio telescopes to extensively test these emission model theories. With observations of more neutron star binary mergers (via triggering on cosmological SGRBs or low redshift gravitational wave events) and careful modelling, we will either detect this emission, be able to show the emission models are incorrect or that the surrounding medium is opaque to coherent radio emission.

ACKNOWLEDGEMENTS

We thank the LOFAR Radio Observatory for implementing the new rapid response mode and for supporting our observations.

RAMJW acknowledges funding from the ERC Advanced Investigator grant no. 247295. RLCS acknowledges support from the ASTRON Helena Kluyver Visitor Programme and from STFC. SM is supported by a PhD studentship awarded by the College of Science and Engineering at the University of Leicester. GEA is the recipient of an Australian Research Council Discovery Early Career Researcher Award (project number DE180100346) funded by the Australian Government.

This paper is based (in part) on data obtained with the International LOFAR Telescope (ILT) under project code LC10_012. LOFAR (van Haarlem et al. 2013) is the Low Frequency Array designed and constructed by ASTRON. It has observing, data processing, and data storage facilities in several countries that are owned by various parties (each with their own funding sources), and that are collectively operated by the ILT foundation under a joint scientific policy.

The ILT resources have benefited from the following recent major funding sources: CNRS-INSU, Observatoire de Paris and Université d'Orlèans, France; BMBF, MIWF-NRW, MPG, Germany; Science Foundation Ireland (SFI), Department of Business, Enterprise and Innovation (DBEI), Ireland; NWO, The Netherlands; The Science and Technology Facilities Council, UK; Ministry of Science and Higher Education, Poland.

This work made use of data supplied by the UK *Swift* Science Data Centre at the University of Leicester and the *Swift* satellite. *Swift*, launched in November 2004, is a NASA mission in partnership with the Italian Space Agency and the UK Space Agency. *Swift* is managed by NASA Goddard. Penn State University controls science and flight operations from the Mission Operations Center in University Park, Pennsylvania. Los Alamos National Laboratory provides gamma-ray imaging analysis.

This research has made use of the NASA/IPAC Extragalactic Database (NED), which is operated by the Jet Propulsion Laboratory, California Institute of Technology, under contract with the National Aeronautics and Space Administration. This research has made use of the SIMBAD data base, operated at CDS, Strasbourg, France.

DATA AVAILABILITY

The data and scripts underlying this article are available in Zenodo at https://doi.org/10.5281/zenodo.3957613. The LOFAR data used are available in the LOFAR Long Term Archive at https://lta.lofar.eu under the Cycle 11 project title LC11_002 with SAS Id numbers 689616 (target data) and 689622 (calibrator data). The *Swift* data used are available from the UK *Swift* Science Data Centre at the University of Leicester at https://www.swift.ac.uk/index.php under GRB 181123B.

REFERENCES

Abbott B. P. et al., 2017, ApJ, 848, L12
Abbott B. P. et al., 2019, ApJ, 875, 160
Ai S., Gao H., Dai Z.-G., Wu X.-F., Li A., Zhang B., Li M.-Z., 2018, ApJ, 860, 57
Alam S. et al., 2015, ApJS, 219, 12
Anderson M. M. et al., 2018, ApJ, 864, 22
Anderson G. E. et al., 2021a, PASA, 38, e026
Anderson G. E. et al., 2021b, MNRAS, 503, 4372
Balsano R. J. et al., 1998, in Meegan C. A., Preece R. D., Koshut T. M., eds, AIP Conf. Proc. Vol. 428, Gamma-Ray Bursts, 4th Hunstville Symposium. Am. Inst. Phys., New York, p. 585
Banagiri S., Coughlin M. W., Clark J., Lasky P. D., Bizouard M. A., Talbot C., Thrane E., Mandic V., 2020, MNRAS, 492, 4945
Barthelmy S. D. et al., 2005, Space Sci. Rev., 120, 143
Beniamini P., Piran T., 2014, MNRAS, 445, 3892
Bloom J. S., Frail D. A., Sari R., 2001, AJ, 121, 2879
Bouwhuis M., Bannister K. W., Macquart J.-P., Shannon R. M., Kaplan D. L., Bunton J. D., Koribalski B. S., Whiting M. T., 2020, MNRAS, 497, 125
Bray J. C., Eldridge J. J., 2016, MNRAS, 461, 3747
Burrows D. N. et al., 2005, Space Sci. Rev., 120, 165
Burrows D. N. et al., 2018, GRB Coordinates Netw., 23435, 1
Carbone D. et al., 2018, Astron. Comput., 23, 92
Cordes J. M., Lazio T. J. W., 2002, preprint (astro-ph/0207156)
Cortiglioni S., Mandolesi N., Morigi G., Ciapi A., Inzani P., Sironi G., 1981, Ap&SS, 75, 153
Dessenne C. A. C. et al., 1996, MNRAS, 281, 977
Dolag K., Gaensler B. M., Beck A. M., Beck M. C., 2015, MNRAS, 451, 4277
Ellingson S. W., Craig J., Dowell J., Taylor G. B., Helmboldt J. F., 2013, preprint (arXiv:1307.0697)
Evans P. A. et al., 2010, A&A, 519, A102
Falcke H., Rezzolla L., 2014, A&A, 562, A137
Fong W., Metzger B. D., Berger E., Özel F., 2016, ApJ, 831, 141
Fong W., Tanvir N. R., Levan A. J., 2018, GRB Coordinates Netw., 23439, 1
Gehrels N. et al., 2004, ApJ, 611, 1005
Gourdji K., Rowlinson A., Wijers R. A. M. J., Goldstein A., 2020, MNRAS, 497, 3131
Hallinan G., 2014, Exascale Radio Astronomy, AAS Topical Conference Series Vol. 2. Proceedings of the conference held 30 March - 4 April, 2014 in Monterey, California. Bulletin of the American Astronomical Society, Vol. 46, p.10203
Hotan A. W. et al., 2014, PASA, 31, e041
Intema H. T., Jagannathan P., Mooley K. P., Frail D. A., 2017, A&A, 598, A78
Inzani P., Sironi G., Mandolesi N., Morigi G., 1982, in Lingenfelter R. E., Hudson H. S., Worrall D. M., eds, AIP Conf. Proc. Vol. 77, Gamma Ray Transients and Related Astrophysical Phenomena. Am. Inst. Phys., New York, p. 79
Ioka K., 2003, ApJ, 598, L79
Kaplan D. L. et al., 2015, ApJ, 814, L25
Kirsten F., Snelders M., Jenkins M., Nimmo K., van den Eijnden J., Hessels J., Gawronski M., Yang J., 2021, preprint (arXiv:2105.11445)
Koranyi D. M., Green D. A., Warner P. J., Waldram E. M., Palmer D. M., 1995, MNRAS, 276, L13
Lasky P. D., Leris C., Rowlinson A., Glampedakis K., 2017, ApJ, 843, L1
Lattimer J. M., Prakash M., 2004, Science, 304, 536
Li Y., Zhang B., 2020, ApJ, 899, L6
Lien A. Y., D'Avanzo P., Palmer D. M., 2018, GRB Coordinates Netw., 23432, 1
Liu L.-D., Gao H., Zhang B., 2020, ApJ, 890, 102
Lorimer D. R., Bailes M., McLaughlin M. A., Narkevic D. J., Crawford F., 2007, Science, 318, 777
Mandhai S., Tanvir N., Lamb G., Levan A., Tsang D., 2019, preprint (arXiv:1908.00100)
Margalit B., Berger E., Metzger B. D., 2019, ApJ, 886, 110
Norris J. P., Barthelmy S. D., Lien A. Y., 2018, GRB Coordinates Netw., 23443, 1
Oates S. R., Lien A. Y., 2018, GRB Coordinates Netw., 23437, 1
Obenberger K. S. et al., 2014, ApJ, 785, 27
Offringa A. R., de Bruyn A. G., Biehl M., Zaroubi S., Bernardi G., Pandey V. N., 2010, MNRAS, 405, 155
Offringa A. R., van de Gronde J. J., Roerdink J. B. T. M., 2012, A&A, 539, A95
Offringa A. R. et al., 2014, MNRAS, 444, 606
Palmer D. M. et al., 2018, GRB Coordinates Netw., 23441, 1
Paterson K., Fong W., 2018, GRB Coordinates Netw., 23440, 1
Paterson K., Fong W., de K., Alexander K., Coppejans D., Hajela A., Margutti R., Terreran G., 2018, GRB Coordinates Netw., 23461, 1
Paterson K. et al., 2020, ApJ, 898, L32
Piro L. et al., 2019, MNRAS, 483, 1912
Pshirkov M. S., Postnov K. A., 2010, Ap&SS, 330, 13
Roming P. W. A. et al., 2005, Space Sci. Rev., 120, 95
Rowlinson A., Anderson G. E., 2019, MNRAS, 489, 3316
Rowlinson A. et al., 2010, MNRAS, 409, 531
Rowlinson A., O'Brien P. T., Metzger B. D., Tanvir N. R., Levan A. J., 2013, MNRAS, 430, 1061
Rowlinson A., Gompertz B. P., Dainotti M., O'Brien P. T., Wijers R. A. M. J., van der Horst A. J., 2014, MNRAS, 443, 1779
Rowlinson A., Patruno A., O'Brien P. T., 2017, MNRAS, 472, 1152
Rowlinson A. et al., 2019, MNRAS, 490, 3483
Salvaterra R., Devecchi B., Colpi M., D'Avanzo P., 2010, MNRAS, 406, 1248
Sarin N., Lasky P. D., Ashton G., 2020, Phys. Rev. D, 101, 063021
Scaife A. M. M., Heald G. H., 2012, MNRAS, 423, L30
Scheers L. H. A., 2011, PhD thesis, Univ. Amsterdam
Shimwell T. W. et al., 2019, A&A, 622, A1
Spitler L. G. et al., 2014, ApJ, 790, 101

Spitler L. G. et al., 2016, Nature, 531, 202
Staley T. D., Fender R., 2016, preprint (arXiv:1606.03735)
Starling R. L. C., Rowlinson A., van der Horst A. J., Wijers R. A. M. J., 2020, MNRAS, 494, 5787
Strateva I. et al., 2001, AJ, 122, 1861
Swinbank J., 2014, Astron. Comput., 7, 12
Swinbank J. D. et al., 2015, Astron. Comput., 11, 25
Taylor J. H., Manchester R. N., Lyne A. G., 1993, ApJS, 88, 529
The CHIME/FRB Collaboration et al., 2020, Nature, 587, 54
Thornton D. et al., 2013, Science, 341, 53
Tingay S. J. et al., 2013, PASA, 30, e007
Totani T., 2013, PASJ, 65, L12
Tunnicliffe R. L. et al., 2014, MNRAS, 437, 1495
Usov V. V., Katz J. I., 2000, A&A, 364, 655
van Haarlem M. P. et al., 2013, A&A, 556, A2
van Weeren R. J. et al., 2016, ApJS, 223, 2
Williams R. D., Seaman R., 2006, in Gabriel C., Arviset C., Ponz D., Enrique S., eds, ASP Conf. Ser. Vol. 351, Astronomical Data Analysis Software and Systems XV. Astron. Soc. Pac., San Francisco, p. 637
Yamasaki S., Totani T., 2020, ApJ, 888, 105
Yi Q. B. et al., 2018, GRB Coordinates Netw., 23452, 1
Zhang B., 2014, ApJ, 780, L21
Zhang B., Mészáros P., 2001, ApJ, 552, L35

This paper has been typeset from a TEX/LATEX file prepared by the author.